JOURNAL OF PROPULSION AND POWER
Vol. 25, No. 6, November–December 2009

Numerical Investigation of Roll Torque Induced by Solid Rocket Motor Internal Flow

Toru Shimada*
Japan Aerospace Exploration Agency, Sagamihara, Kanagawa 229-8510, Japan
and
Nobuhiro Sekino† and Mihoko Fukunaga‡
IHI Aerospace Company, Ltd., Tomioka, Gunma 370-2398, Japan

DOI: 10.2514/1.40281

To understand the mechanism of the generation of large roll torque in an operating solid rocket motor with axially slotted propellant grain and a narrow nozzle-submergence region, fully three-dimensional Navier–Stokes numerical simulations are conducted. Several grain configurations are computed, and it is found that there are at least two groups of quasi-steady-state solutions: one shows large roll torque, and the other shows small roll torque. From the current simulation results, it is observed that large roll torque is generated as a result of the interaction of the circling flow around the nozzle inlet with the slot jet exhausting from the slot end into the aft-end cavity. Although the roll torque evaluated from the computation is one order higher than that observed in real fight, the simulations provide an insight into the qualitative mechanism of real roll-torque generation.

Nomenclature

A, B, C	=	inviscid flux Jacobian matrices
c	=	specific heat of condensed phase
e	=	total energy per unit volume
$\overleftrightarrow{I}$	=	unit matrix
i, j, k	=	cell indices
p	=	pressure
$\mathbf{Q}$	=	conserved variable vector
$\mathbf{q}$	=	heat flux vector
R	=	gas constant
$\bar{R}$	=	effective gas constant
t	=	time from ignition
u, v, w	=	velocity components in x, y, z directions, respectively
$\mathbf{V}$	=	velocity vector
$\bar{\gamma}$	=	effective specific heat ratio
γ_g	=	specific heat ratio of gas
Δt	=	local time step
ν_A, ν_B, ν_C	=	spectral radii of A, B, C
ρ	=	density
$\overleftrightarrow{\tau}$	=	stress tensor
ψ	=	loading ratio

I. Introduction

FROM the pioneering days of modern rocketry, it has been recognized and reported that roll torque is generated around the thrust axis during the firing of a solid rocket without tail fins, especially with relation to acoustic instability in the combustion chamber of a solid rocket motor (SRM) [1–6].

As in the case of the first launch of the Sergeant missile in 1961 [4], or as in some other cases, the intensity of the roll torque generated is sometimes one order higher than that expected from the aerodynamics and thrust misalignment. This roll torque tends to occur during the early period of the burn and then tends to decline.

The mechanism of roll-torque generation, in general, is categorized into several types, including acoustic instability, grain configuration, nozzle erosion, and jet damping (of a spinning motor) [7]. However, a method has not yet been established to predict the amount of possible roll-torque generation when an individual SRM specification is given. It seems therefore, that, even in recent years, in the system design of launch vehicles (LVs), one cannot help but employ some empirical evaluation [7].

In a situation where a booster is used as the first-stage motor, such as the planned U.S. ARES-1 crew LV [8,9], or where a new launch system is constructed of new SRMs, such as the European VEGA LV [10,11], there is a pressing need in the design phase for an evaluation of the amount of torque. Against such a background, there is a need worldwide for clarification regarding the origin and mechanism of the generation of roll torque of an SRM during its operation.

The Mu-V LV (M-V) [12,13] is a Japanese three-stage, full solid-propellant rocket system, which was launched seven times from 1997 to 2006. As reported recently [14,15], marked roll-torque disturbance was observed during the first-stage motor burn in all M-V flights. The roll-torque disturbance estimated from the attitude-angle measurement is plotted in Fig. 1. The strength of the torque is more than 3 kN · m immediately after separation from the launcher, and it then attenuates gradually. It is a high, but transient, torque, so that the roll-control system can handle it without any problem. As for the direction of the torque, it was observed to have the same direction in six flights out of seven. The peak value of the measured torque is an order of magnitude higher than that estimated from the aerodynamics and thrust misalignment. With regard to this roll torque, a theoretical evaluation has been made and a fully three-dimensional computational fluid dynamics (CFD) simulation of the flow inside the combustion chamber has been reported [14,15].

The major objective of this paper is to investigate the flowfield inside a motor chamber with axial slots and in the aft cavity of the nozzle-submergence region based on CFD simulations. It should be noted that the nozzle treated is not canted. Moreover, we will discuss how roll torque and side thrust change according to grain shape, by comparing numerical solutions for several grain burnback configurations. The grain configuration dealt with in this study is generic as a star-perforated motor, but its shape and size are basically similar to a

Presented as Paper 4891 at the 44th AIAA/ASME/SAE/ASEE Joint Propulsion Conference & Exhibit, Hartford, CT, 21–23 July 2008; received 6 August 2008; revision received 23 July 2009; accepted for publication 23 July 2009.

*Professor, Department of Space Transportation Engineering, Institute of Space and Astronautical Science, 3-1-1 Yoshinodai. Senior Member AIAA.
†General Manager, Technologies Development Department, 900 Fujiki.
‡Manager, Technologies Development Department, 900 Fujiki.

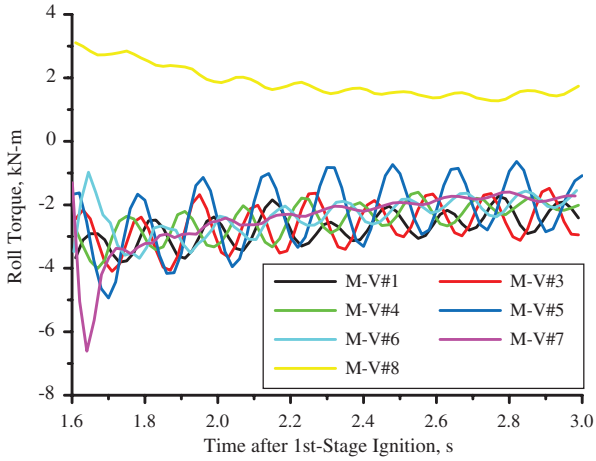

Fig. 1 Roll torque observed in M-V flights [14].

real motor (M-14, the first-stage motor of an M-V). Therefore, at least a qualitative comparison of roll torque is thought possible between the simulation and the flight data.

II. Numerical Analysis

A. Assumptions

Although the nature of particle-gas multiphase flow in an SRM is important for a perfect understanding of the phenomena, it is considered here that the assumption of an equilibrium two-phase flow is useful for the purpose of this paper. Therefore, it is assumed that there is no lag in velocity and in temperature between the particle and the gas. The propellant is assumed to be composed of AP/HTPB/AL with weight percentages of 68/12/20, respectively, with a small amount of Fe_2O_3. The chemical composition of the gas mixture including liquid Al_2O_3 is evaluated at chamber condition using a chemical equilibrium code, and is assumed to be frozen in the flowfield. These two assumptions make it possible to formulate the problem by the flow of a fictitious single-species gas with effective specific heat and mean molecular weight. It is assumed that the transport coefficients of the gas mixture can be expressed by the power function of the temperature. The gas is assumed to follow the ideal gas equation of state.

B. Grain Configuration

At the time of ignition ($t = 0$ s), the center bore of a generic SRM is assumed to be 9400 mm in length, 640 mm in diameter, and have seven axial slots along the entire length. Each slot is 140 mm in width and 480 mm in depth. The grain configuration is shown in Fig. 2. The nozzle of the SRM is submerged in and connected to the aft dome of the motor. The throat diameter is 750 mm. The nozzle exit cone has a half-angle of 15 deg, and the area ratio is 10.

Considering that the grain configuration changes along with the progression of combustion, flowfields with four grain shapes, at the initial, 1.6 s burnback, 3 s burnback, and 5 s burnback, are computed. Although in reality the thermal protection system surface recedes, the effect of it is out of the scope of this paper.

C. Governing Equations

The governing equations are 3-D unsteady compressible Navier–Stokes equations. Neither a turbulent model nor a subgrid scale model is implemented. The simulation can directly analyze the eddies of a size that the current grid system can resolve. On the other hand, subgrid scale phenomena are not treated by an explicit model. Numerical diffusion due to a third-order upwind scheme is thought to play a similar role somehow.

The governing equations for mass, momentum, and energy can be written as follows:

$$\frac{\partial \rho}{\partial t} + \nabla \cdot (\rho \mathbf{V}) = 0 \tag{1}$$

$$\frac{\partial \rho \mathbf{V}}{\partial t} + \nabla \cdot (\rho \mathbf{V} \otimes \mathbf{V} + p\overleftrightarrow{I} - \overleftrightarrow{\tau}) = 0 \tag{2}$$

$$\frac{\partial e}{\partial t} + \nabla \cdot [e\mathbf{V} + (p\overleftrightarrow{I} - \overleftrightarrow{\tau}) \cdot \mathbf{V} - \mathbf{q}] = 0 \tag{3}$$

where ρ is density, $\mathbf{V}$ is velocity, p is pressure, $\overleftrightarrow{\tau}$ is the stress tensor, e is the total energy per unit volume, and $\mathbf{q}$ is the heat flux vector due to thermal conduction. Total energy per unit volume can be expressed as

$$e = p/(\bar{\gamma} - 1) + \rho |\mathbf{V}|^2/2 \tag{4}$$

and the equation of state for the ideal gas as

$$p = \rho \bar{R} T \tag{5}$$

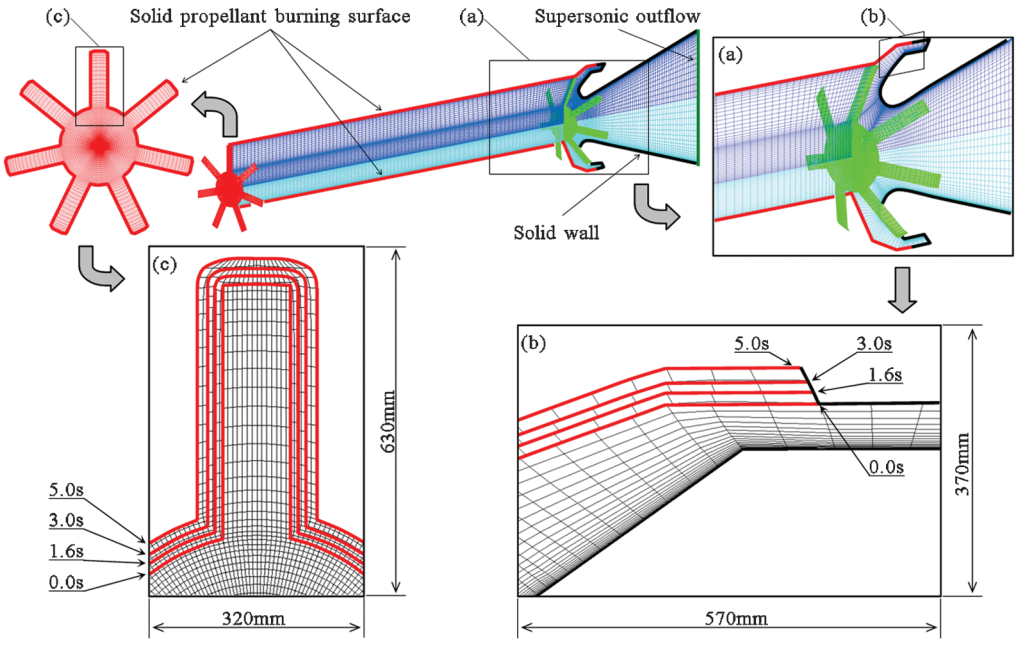

Fig. 2 Multiblock computational grids for four time levels of 0, 1.6, 3.0, and 5.0 s, with description of applied conditions on the grid boundaries.

For the equilibrium two-phase gas flow, the effective gas constant and the effective specific heats ratio are determined as follows:

$$\frac{1}{\bar{\gamma}-1}=\frac{1}{\gamma_g-1}+\frac{\psi c}{R} \tag{6}$$

$$\bar{R}=\frac{R}{1+\psi} \tag{7}$$

where ψ is the ratio of the particle bulk density to gas density, or loading ratio, γ_g is the specific heat ratio of the gas phase, R is the gas constant, and c is the specific heat of the condensed phase.

D. Computational Fluid Dynamics Analysis

The CFD code employed in this study is W-Master, which was first developed in the late 1980s and has been updated and validated through various aerospace, basically SRM-related, applications. It is a finite volume, multiblock CFD solver for 3-D compressible Navier–Stokes equations. In the finite volume method, cell-averaged values of conservation variables are updated time dependently for each cell by estimating the net amount of the mass, momentum, and energy flows across its surrounding interfaces with neighboring cells. General complex geometry can be handled by its multiblock structured grid approach. Detailed descriptions of the numerical methods employed in the solver are available in literature [16].

The computational region is bounded by propellant grain and the surface of the nozzle inner wall, the center axis of the motor and the nozzle, the exit plane of the nozzle exit cone, and the boundary planes of the periodical conditions in the circumferential direction. The grid system is shown in Fig. 2. The number of grid points are $152 \times 151 \times 211$ (equal to 4.842872×10^6). The minimum grid spacing on the nozzle surface is 0.1 μm, which is small enough for the viscous sublayer over the surface to be resolved.

The boundary condition on the inert wall is a nonslip condition with a fixed wall temperature of 2500 K. On the burning surface, the temperature is fixed at 3500 K, the pressure is extrapolated from the adjacent cell, and the velocity direction is normal to the surface. The mass flux through the surface is determined by multiplying the propellant density by the linear burning rate evaluated by Vieille's law. It is assumed that the linear burning rate of the propellant is 9 mm/s at a pressure of 5 MPa. The erosive burning effect is not considered in this study. On the azimuthal boundaries, periodic boundary conditions are imposed, and on the nozzle exit plane, so are supersonic outflow conditions. On the axis of revolution, the surface area diminishes on the axis and the net flows of the mass, momentum, and energy across the axis are precisely zero.

In this study, we seek the (quasi) steady state of a large-scale flow structure for each considered grain configuration. In reality, after ignition, it takes about 0.5 s to fill the combustion chamber, and so it is not realistic to consider the steady state at $t = 0$. It is, therefore, not within the scope of this study to simulate the temporal development of the internal flow during the ignition transient and afterward. The current objective is to see how the large-scale structure of the flow will be at the "infinity" of time if the grain shape stays the same.

In this case, the steady-state solution may be different if the initial condition is different, as a result of the nonlinear nature of fluid flow. The initial condition is set so that the estimated chamber conditions are given in the combustion chamber, and so are the estimated nozzle flow conditions (isentropic) in the nozzle region. No circumferential disturbance is applied.

In addition, the steady-state solution may be different if the numerical integration scheme is different or if the grid system is different. We have used two time-stepping selections as described in the next section.

E. Lower-Upper Symmetric Gauss–Seidel Scheme with Implicit Periodic Boundary Conditions

The system of the algebraic equations for the (i, j, k)th cell can be formally written by integrating the governing equations over cell volume (Vol) and (local) time step Δt as

$$\mathrm{Vol}\,\frac{\Delta \mathbf{Q}}{\Delta t}+\delta\mathbf{E}+\delta\mathbf{F}+\delta\mathbf{G}=\delta\mathbf{E}_\mathbf{V}+\delta\mathbf{F}_\mathbf{V}+\delta\mathbf{G}_\mathbf{V} \tag{8}$$

where $\Delta\mathbf{Q}=\mathbf{Q}^{n+1}-\mathbf{Q}^n$ is the temporal change of the conserved variable vector $\mathbf{Q}=[\rho \quad \rho u \quad \rho v \quad \rho w \quad e]^t$, and $\delta\mathbf{E}$, $\delta\mathbf{F}$, and $\delta\mathbf{G}$ are the differences of the inviscid flux vectors integrated over the area of the cell faces of the i direction, j direction, and k direction, respectively. Similarly, $\delta\mathbf{E}_\mathbf{V}$, $\delta\mathbf{F}_\mathbf{V}$, and $\delta\mathbf{G}_\mathbf{V}$ are the viscous counterparts.

The standard lower-upper symmetric Gauss–Seidel (LU-SGS) numerical time integration for the (i, j, k)th cell can formally be written as

$$\left[I-\frac{1}{\alpha}\left(A^+_{i-1,j,k}+B^+_{i,j-1,k}+C^+_{i,j,k-1}\right)\right]\times\left[I+\frac{1}{\alpha}\left(A^-_{i+1,j,k}+B^-_{i,j+1,k}+C^-_{i,j,k+1}\right)\right]\Delta\mathbf{Q}=\mathbf{RHS} \tag{9}$$

$$\mathbf{RHS}=-\frac{1}{\alpha}\left(\delta\mathbf{E}+\delta\mathbf{F}+\delta\mathbf{G}-\delta\mathbf{E}_\mathbf{V}-\delta\mathbf{F}_\mathbf{V}-\delta\mathbf{G}_\mathbf{V}\right)^n \tag{10}$$

$$\alpha=\nu_A+\nu_B+\nu_V+\alpha_V+\frac{\mathrm{Vol}}{\Delta t} \tag{11}$$

where A, B, and C are the inviscid flux Jacobian matrices integrated over the cell surfaces. They are split into two matrices with superscripts $\pm$ denoting plus and minus eigenvalues and with definition $A^\pm=(A\pm\nu_A I)/2$, and so on. Note that the spectral radii ν_A, ν_B, and ν_C include the cell-surface areas of the respective directions. The viscous effect is counted by α_V.

The LU-SGS scheme has good stability characteristics for a large time step, even for the limit of $\Delta t\to\infty$. We have employed two types of time step to obtain quasi-steady-state solutions. One is Eq. (11) itself, with the local time step at each cell evaluated to satisfy the Courant number be unity, and the other is the limit form of Eq. (11) when $\Delta t\to\infty$ with, in practice, a factor a little larger than unity multiplied to α.

In this study, we are interested in the stability of the pairs of counter-rotating vortices in the circumferential direction. It is necessary to treat a full 360 deg to clarify this by numerical simulation without the numerical disturbances at the boundaries where the periodic boundary conditions should be implied. Although it is often the case with an LU-SGS scheme seeking a steady-state solution that the explicit boundary condition, that is, $\Delta\mathbf{Q}_{i,j,nk}=\Delta\mathbf{Q}_{i,j,0}=0$, is employed at the ghost cell adjacent to the boundary, the implicit treatment is indispensable at the periodic boundaries for that reason, in this case. The implicit periodic boundary conditions can be written as

$$\Delta\mathbf{Q}_{i,j,nk}=\Delta\mathbf{Q}_{i,j,1}\qquad\Delta\mathbf{Q}_{i,j,0}=\Delta\mathbf{Q}_{i,j,nk-1} \tag{12}$$

With $\Delta\bar{\mathbf{Q}}$ denoting the part of the second half of the left-hand side of Eq. (9), it can be written as

$$\left[I-\frac{1}{\alpha}\left(A^+_{i-1,j,k}+B^+_{i,j-1,k}+C^+_{i,j,k-1}\right)\right]\Delta\bar{\mathbf{Q}}=\mathbf{RHS} \tag{13}$$

or

$$\Delta\bar{\mathbf{Q}}_{i,j,k}-\frac{A^+_{i-1,j,k}}{\alpha_{i,j,k}}\Delta\bar{\mathbf{Q}}_{i-1,j,k}-\frac{B^+_{i,j-1,k}}{\alpha_{i,j,k}}\Delta\bar{\mathbf{Q}}_{i,j-1,k}-\frac{C^+_{i,j,k-1}}{\alpha_{i,j,k}}\Delta\bar{\mathbf{Q}}_{i,j,k-1}=\mathbf{RHS}_{i,j,k} \tag{14}$$

By transposing the A and B terms to the right-hand side, and then redenoting it by $\boldsymbol{\psi}$, we get

$$\Delta\bar{\mathbf{Q}}_{i,j,k}-\frac{C^+_{i,j,k-1}}{\alpha_{i,j,k}}\Delta\bar{\mathbf{Q}}_{i,j,k-1}=\mathbf{RHS}_{i,j,k}+\frac{A^+_{i-1,j,k}}{\alpha_{i,j,k}}\Delta\bar{\mathbf{Q}}_{i-1,j,k}+\frac{B^+_{i,j-1,k}}{\alpha_{i,j,k}}\Delta\bar{\mathbf{Q}}_{i,j-1,k}\equiv\boldsymbol{\psi}_{i,j,k} \tag{15}$$

For each set of i and j, we get the following equation by successive substitution of the terms into the equation of $k = nk-1$ down to $k = 1$, omitting the subscripts i, j:

$$\Delta\bar{\mathbf{Q}}_{nk-1} = \boldsymbol{\psi}_{nk-1} + \boldsymbol{\psi}_{nk-2}\frac{C^+_{nk-2}}{\alpha_{nk-1}} + \cdots + \boldsymbol{\psi}_2\frac{\prod_{k=2}^{nk-2} C^+_k}{\prod_{k=3}^{nk-1}\alpha_k} + \frac{\prod_{k=1}^{nk-2} C^+_k}{\prod_{k=2}^{nk-1}\alpha_k}\left[\boldsymbol{\psi}_1 + \frac{C^+_{nk-1}}{\alpha_1}\Delta\bar{\mathbf{Q}}_{nk-1}\right] \tag{16}$$

This equation can be written as

$$\left[I - \frac{\prod_{k=1}^{nk-1} C^+_k}{\prod_{k=1}^{nk-1}\alpha_k}\right]\Delta\bar{\mathbf{Q}}_{nk-1} = \boldsymbol{\psi}_{nk-1} + \sum_{\ell=1}^{nk-2}\left[\frac{\prod_{k=\ell}^{nk-2} C^+_k}{\prod_{k=\ell+1}^{nk-1}\alpha_k}\boldsymbol{\psi}_\ell\right] \tag{17}$$

and, by solving the preceding equation, we get $\Delta\bar{\mathbf{Q}}_{nk-1}$, namely, $\Delta\bar{\mathbf{Q}}_0$.

The part of the second operator can be

$$\left[I + \frac{1}{\alpha}(A^-_{i+1,j,k} + B^-_{i,j+1,k} + C^-_{i,j,k+1})\right]\Delta\mathbf{Q} = \Delta\bar{\mathbf{Q}}_{i,j,k} \tag{18}$$

or

$$\Delta\mathbf{Q}_{i,j,k} + \frac{C^-_{i,j,k+1}}{\alpha_{i,j,k}}\Delta\mathbf{Q}_{i,j,k+1} = \Delta\bar{\mathbf{Q}}_{i,j,k} - \frac{A^-_{i+1,j,k}}{\alpha_{i,j,k}}\Delta\mathbf{Q}_{i+1,j,k} - \frac{B^-_{i,j+1,k}}{\alpha_{i,j,k}}\Delta\mathbf{Q}_{i,j+1,k} \equiv \boldsymbol{\Phi}_{i,j,k} \tag{19}$$

By a similar operation, omitting the subscripts i, j, we can get the following equation, and by solving it we can obtain $\Delta\mathbf{Q}_1$, namely, $\Delta\mathbf{Q}_{nk}$:

$$\left[I - (-1)^{nk-1}\frac{\prod_{k=1}^{nk-1} C^-_k}{\prod_{k=1}^{nk-1}\alpha_k}\right]\Delta\mathbf{Q}_1 = \boldsymbol{\Phi}_1 + \sum_{\ell=2}^{nk-1}\left[(-1)^{\ell-1}\frac{\prod_{k=2}^{\ell} C^-_k}{\prod_{k=1}^{\ell-1}\alpha_k}\boldsymbol{\Phi}_\ell\right] \tag{20}$$

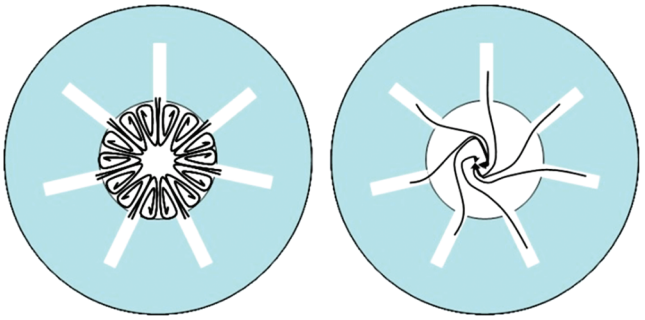

Fig. 3 Illustration of the vortical flow patterns (thought experiment).

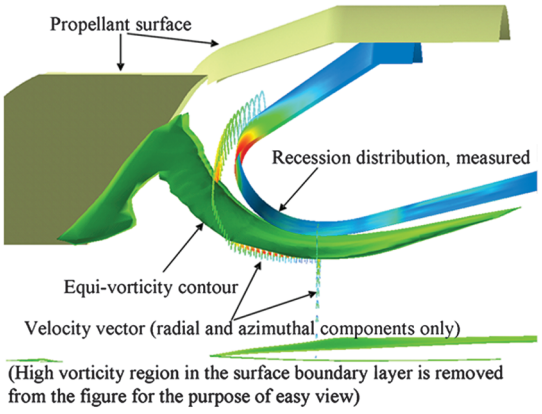

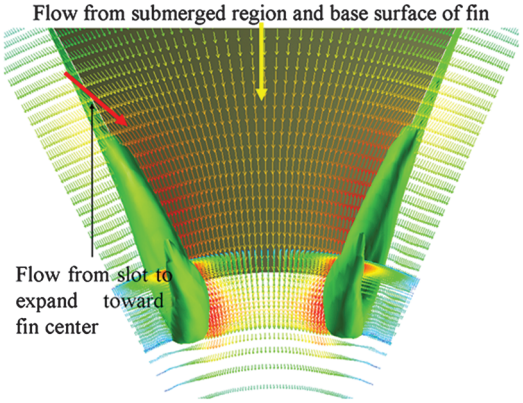

Fig. 4 Vortical flow tube in the aft-end cavity region (from [16]).

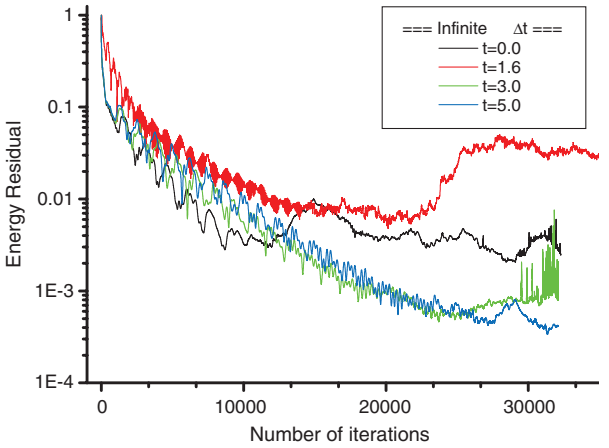

Fig. 5 Residual histories of computations ($\Delta t \to \infty$).

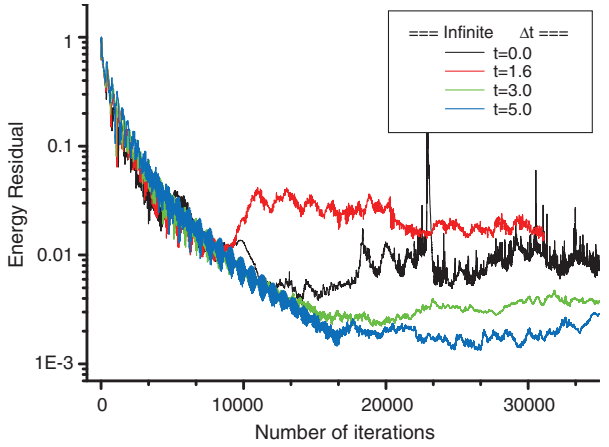

Fig. 6 Residual histories of computations (local time step).

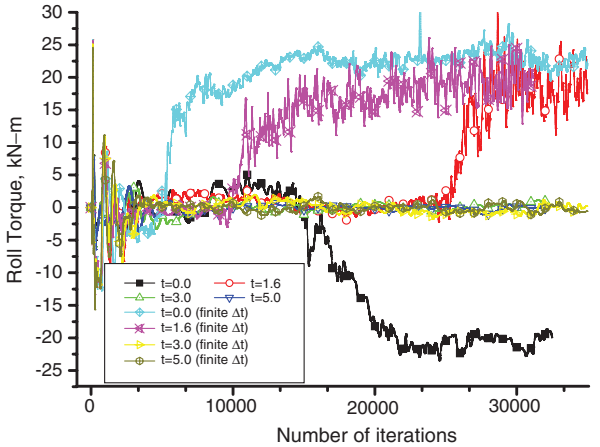

Fig. 7 Roll-torque convergence history.

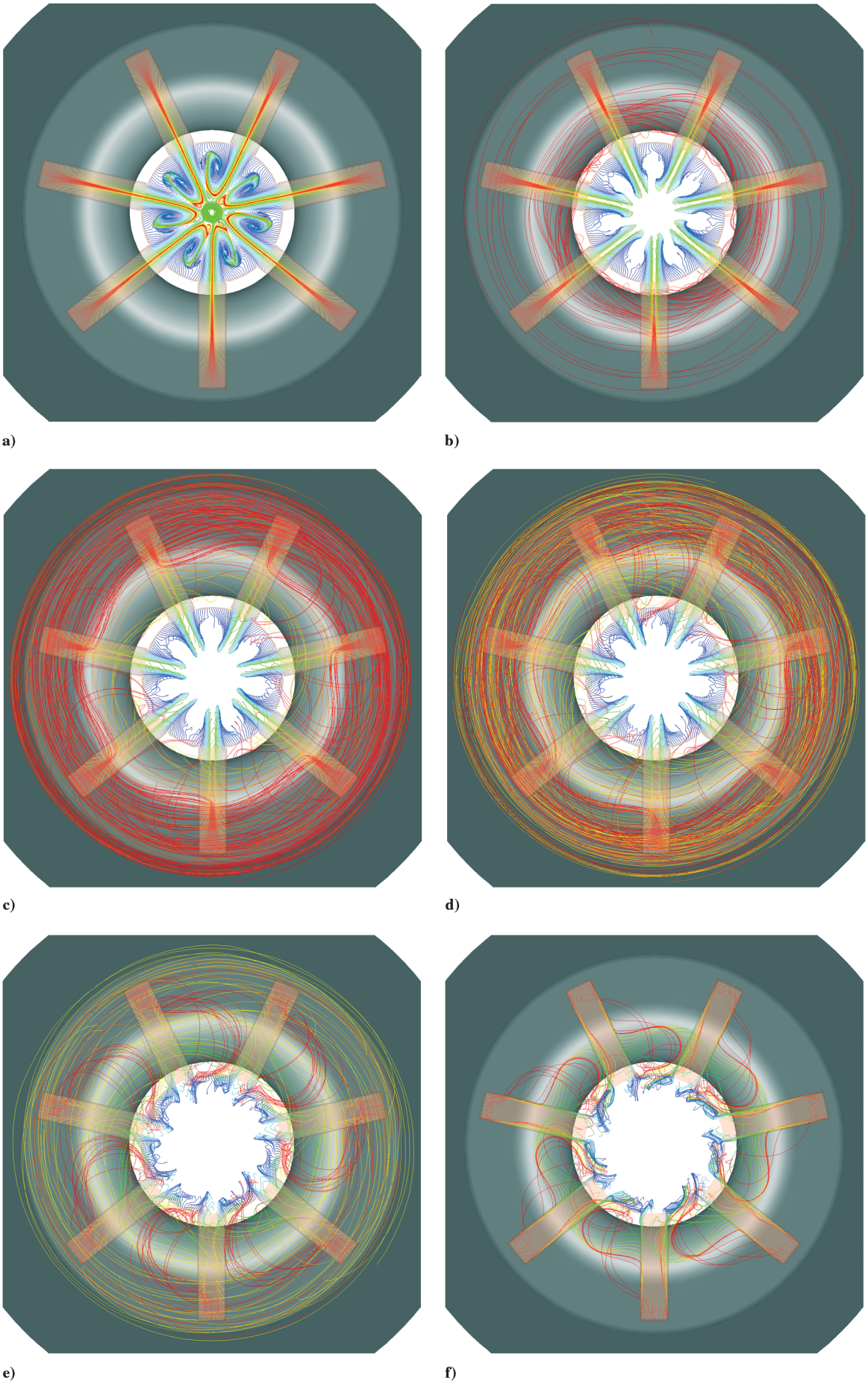

Fig. 8 Colored stream lines shed from the burning surface at representative axial locations, $t = 0$ s (view from $x = -\infty$): a) $x/L = 0.015$, b) $x/L = 0.30$, c) $x/L = 0.40$, d) $x/L = 0.50$, e) $x/L = 0.74$, f) $x/L = 0.94$.

III. Results and Discussion

A. Thought Experiment and Previous Numerical Evidence

1. Thought Experiment

In the cross section of a port, because mass efflux is accumulated in the slots, a jet will flow into the main port from each slot. What kind of flow will these seven jets generate inside the port? Simply put, the result of this thought experiment can be divided into at least two cases: the symmetrical type and the asymmetrical type, as shown in Fig. 3. A case in which there is no torque occurs only when there is a steady flow creating seven pairs of vortices in symmetrical form.

2. Previous Numerical Evidence

From a previous numerical study by the authors' group, it is suggested that there will be pairs of vortical flow tubes generated from the bottom surface of the grain in the aft-end cavity region (nozzle-submergence region). That simulation was conducted over one-seventh of the entire circumference. Figure 4 shows simulation results taken from [16]. The vortical flow is generated due to the high mass flux of the flow coming out of the slot exit facing the aft-end cavity. The vortical flow tubes are counter-rotating each other, but have equal strength, namely, they are symmetric about the center plane. It is probable that a symmetric solution is obtained due to the limitation of circumferential freedom.

B. Convergence History of Simulation

We have conducted four cases: $t = 0$ s, $t = 1.6$ s, $t = 3$ s, and $t = 5$ s. The normalized energy residual is shown in Fig. 5 for the infinite time-step solutions, and so is in Fig. 6 for the local time-step solutions. The total energy residual is calculated in the following way:

$$E_{\text{res}} = \sqrt{\frac{\sum_{i,j,k} (e^{n+1}_{i,j,k} - e^{n}_{i,j,k})^2 \text{Vol}_{i,j,k}}{\sum_{i,j,k} \text{Vol}_{i,j,k}}} \tag{21}$$

Typically, it takes about 1 min of CPU time to calculate the amount of procedures for one time step. From Fig. 5, we see clearly the convergence of the flowfield up to 12,000 iterations for all cases. For the case of $t = 0$, the residual stops decreasing afterward. As for the case of $t = 1.6$, a change of the convergence tendency appears after 20,000 steps. As for the case of $t = 3.0$, we have good convergence history up to 25,000 steps, but after that it stops decreasing, and we see some instability at around 30,000 steps. Finally, in the case of $t = 5.0$, we get a good convergence up to 32,000 steps and more than a 3-orders-of-magnitude decrement of the residual is seen.

From Fig. 6, we see the residual histories for the cases of finite local time steps.

C. Roll-Torque Evaluation

When the internal flow reaches a steady state or quasi-steady-state, then the roll torque acting on the SRM can be evaluated by integrating the axial component of the angular-momentum flux over the nozzle exit plane and changing the sign, that is,

$$T = -\iint_{\text{Nozzle Exit}} \rho u (y \cdot w - z \cdot v)\, \mathrm{d}S \tag{22}$$

In Fig. 7, the computed values of T are plotted against the iteration number of the CFD simulation. From this figure, one can read the level of roll torque and the extent of the steadiness of the computation. The value of T shows low-frequency oscillatory behavior with zero as the average in the earlier period of the simulation. Then, in the later period, the average shifts to a large value for the cases of $t = 0$ s and $t = 1.6$ s. The case of $t = 0$ s has two solutions: one is positive torque, and the other is negative. It seems that the direction of the torque is numerically ad hoc; the trigger for the circling flow growth is probably due to accumulation of numerical error of small quantity. The circling flow does not change its direction once it grows up to a limit-cycle. About the cases where $t = 3$ s and $t = 5$ s, the roll torque is small, practically zero, compared to the others.

The magnitude of the quasi-steady roll torque is about 20 kN · m, which is very high compared to the roll torque estimated using M-V

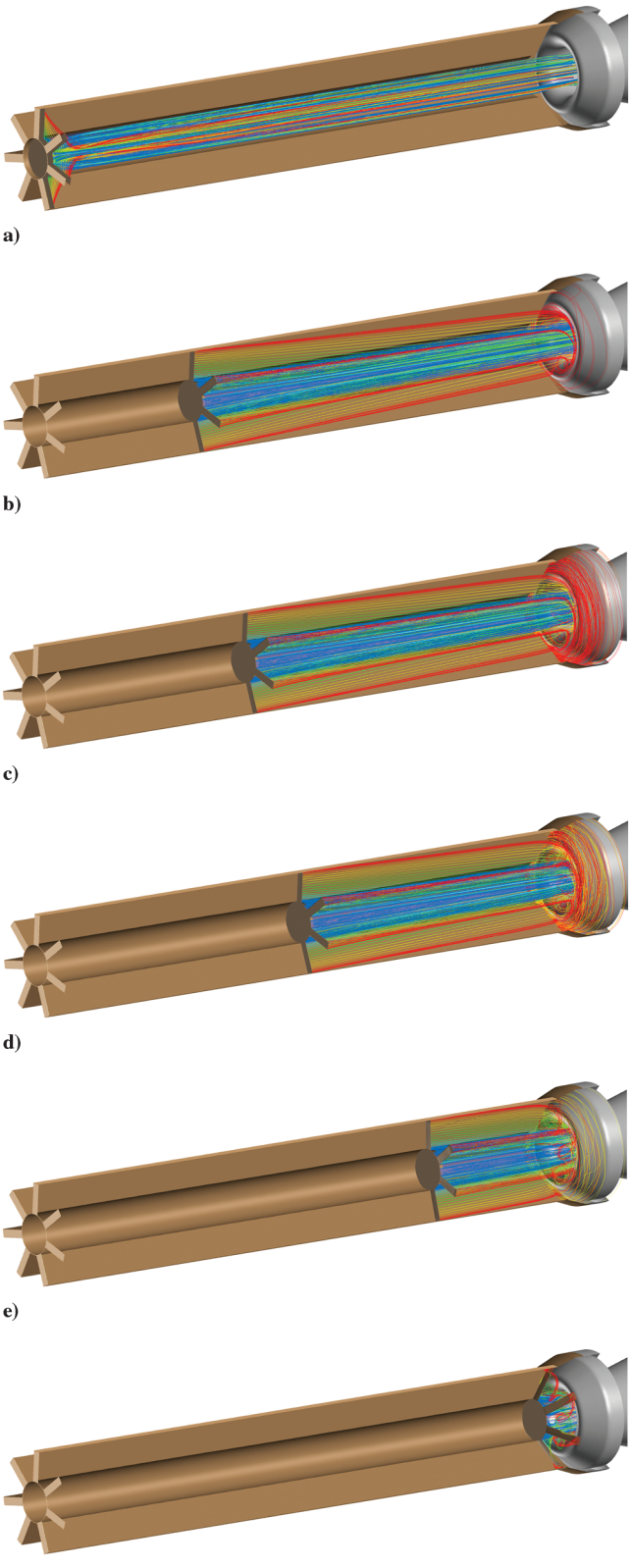

Fig. 9 Colored stream lines shed from the burning surface at representative axial locations, $t = 0$ s (perspective view): a) $x/L = 0.015$, b) $x/L = 0.30$, c) $x/L = 0.40$, d) $x/L = 0.50$, e) $x/L = 0.74$, f) $x/L = 0.94$.

flight data. The difference can be attributed to the fact that the current simulation is for a fully developed quasi-steady flow for a fixed geometry; on the other hand, in a real situation, there is an unsteady ignition transient, the grain burnback is continuous, the solid-propellant grain is not a rigid body, the flow has condensed-phase droplets, and so on. In spite of the many differences between the computation and the reality, we believe that we can discuss the origin of the large roll torque that occurs in this type of motor, at least qualitatively.

We could also evaluate the torque and force the other way, that is, by integrating the inviscid and the viscous momentum fluxes over the internal surfaces. The roll torque, so evaluated, shows a similar value to the aforementioned. The side force is 0.3% of the axial thrust for the large-torque case and 0.02% for the small-torque case. The viscous contribution to total roll torque is typically 1.0% for the large-torque case. Therefore, the basic mechanism of the roll torque here is considered as an inviscid phenomenon, that is, the moment of the pressure force.

Hereafter, we would like to discuss the cases of $t = 0$ s and $t = 5$ s, respectively, as representative of the large and the small-torque results. The time stepping for these is the infinite time step.

D. Flowfield of Large-Torque Generation

In Fig. 8, colored streamlines shed from the propellant burning surface at representative axial locations, expressed by the ratio x/L, where L is the length between the nozzle throat and the head end of the motor, and x is the length from the head end, which are shown in the view as seen from $x = -\infty$. Also, in Fig. 9, the perspective views of these are shown.

At the upstream, shown in Figs. 8a and 9a for $x/L = 0.015$, are streamlines from three types of swirling flows. One is a clockwise-rotating single vortex tube around the center axis. This vortex tube consists almost solely of streamlines (colored green) shed from the part at an intermediate depth of one of the side walls. The second is the clockwise-rotating flow consisting of streamlines (colored blue) shed from the burning surfaces directly facing the bore and the streamlines shed from a part of the side wall in the slot (colored from green to blue). There are seven vortical flow tubes corresponding to the number of slots. The third is a small counterclockwise-rotating small vortical flow located between the aforementioned two types. Mainly, this consists of the stream coming from the deepest part (bottom) of the slot (colored red) and that from the bottom to the intermediate-deep part of the both side walls (colored red to yellow).

In Figs. 8b and 9b, the streamlines shed from the $x/L = 0.3$ location are shown. It can be seen that the streamlines shed from the bottom of the slot (colored red) do not flow into the bore, but flow into the aft-end cavity through the slot exit and, moreover, they circle around the nozzle inlet in a clockwise direction. On the other hand, the streamlines shed from the other region of the slot do not form a spiral flow and flow into the bore almost in the same circumferential phase. The stream (colored blue) from the surface facing the bore flows around the vortex tube generated upstream.

In Figs. 8c and 9c, the streamlines from $x/L = 0.4$ are shown. In comparison with Figs. 8b and 9b, the space in the slot occupied by the stream from the upstream widens. Because of this, the stream from the bottom of the slot flows into the aft cavity at the intermediate depth of the slot. Because it enters the cavity at a high radial position, the residence time in the submergence region becomes larger in comparison with Figs. 8b and 9b. The other streamlines show basically the same feature as Figs. 8b and 9b. In Figs. 8d and 9d, the same feature can be seen with more streamlines from the side walls (colored yellow).

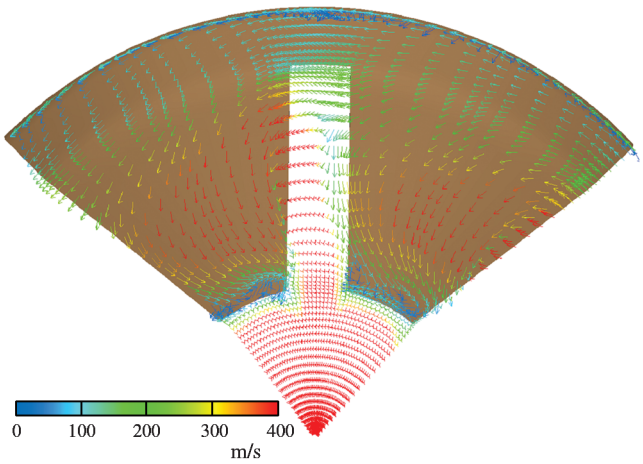

Fig. 10 Velocity field in the interfacing surface between the aft-end cavity and the propellant grain, $t = 0$ s.

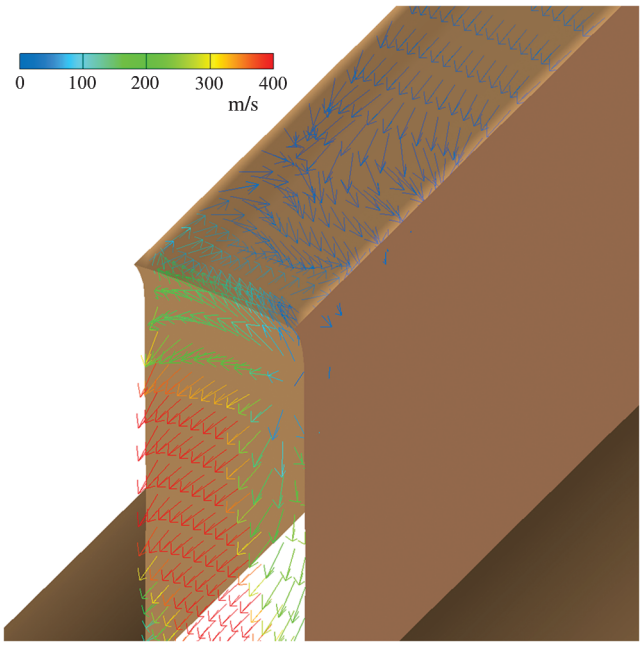

Fig. 11 Velocity distribution near the slot exit to the aft-end cavity, $t = 0$ s.

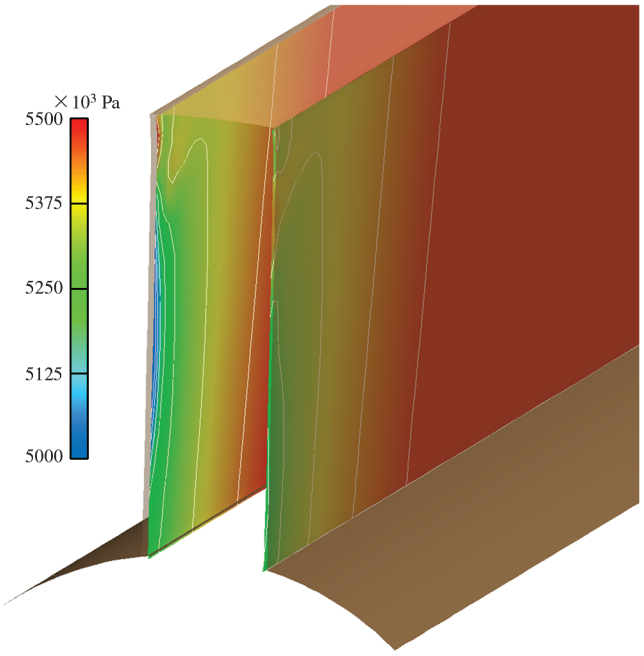

Fig. 12 Pressure distribution near the slot exit to the aft-end cavity, $t = 0$ s.

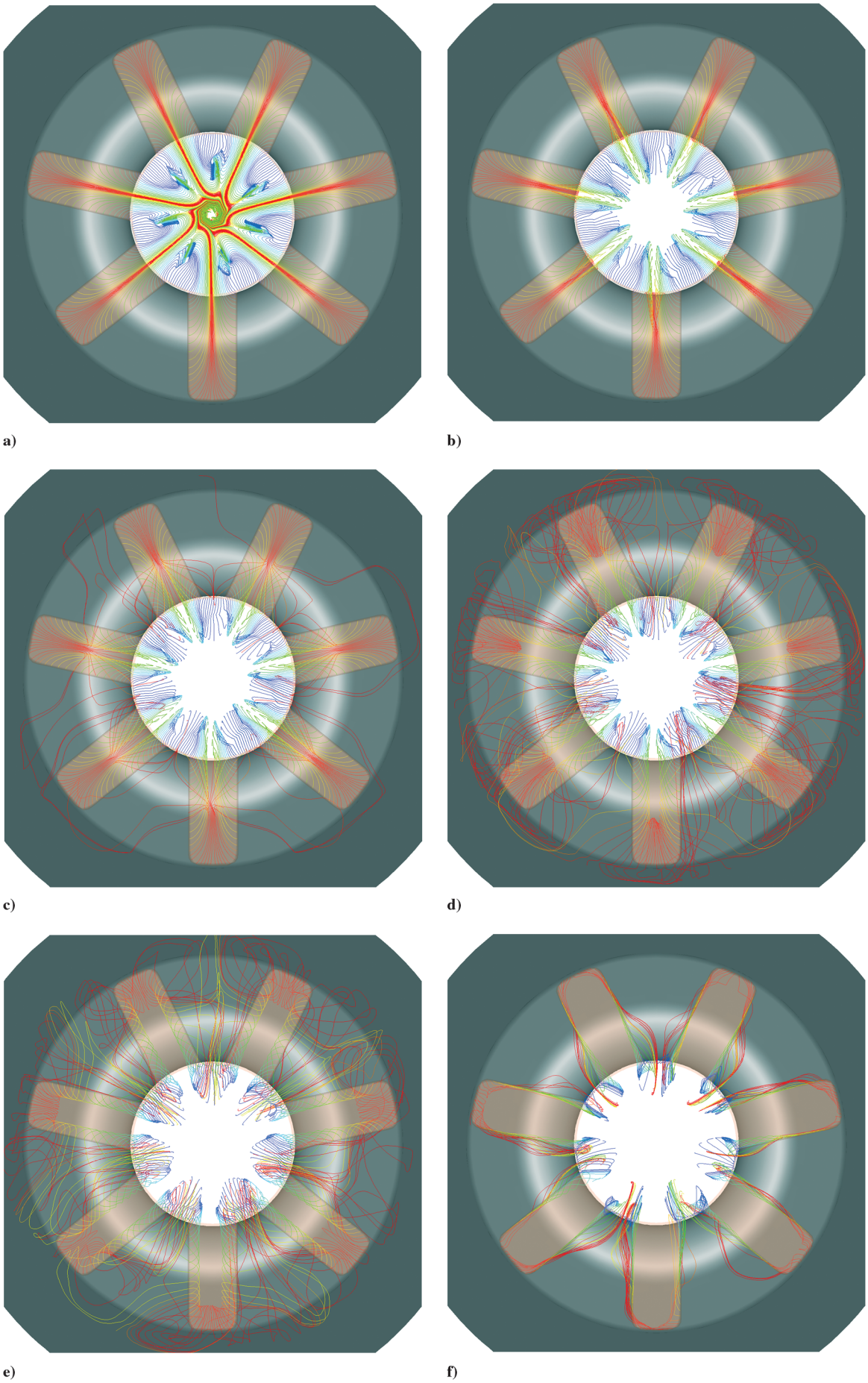

Fig. 13 Colored stream lines shed from the burning surface at representative axial locations, $t = 5$ s (view from $x = -\infty$): a) $x/L = 0.015$, b) $x/L = 0.30$, c) $x/L = 0.40$, d) $x/L = 0.50$, e) $x/L = 0.74$, f) $x/L = 0.94$.

In Figs. 8e, 8f, 9e, and 9f, the streamlines shed from the bottom or the deep part interact with the jet exhaust from the bottom end of the slot to the aft cavity, so that they cannot circle around the nozzle inlet, but they flow around in one segment of the grain bottom surface between the neighboring slot exit. This circling flow and slot jet interaction creates an imbalance in the pressure and velocity fields at the adjacent region of the slot exit facing the aft-end cavity.

As shown in Fig. 10, the circling flow is formed at a large radius over the propellant surface, and this flow interacts with the jet coming out of the slot. First, the circling flow hits the wall of the slot side wall at the deep location shown in Fig. 11. Upon the impingement of flow, a reverse flow is observed at the slot bottom facing the cavity. This reverse flow collides with the flow coming from the upstream and, naturally, it forms a circulating region. The returning flow comes out along the right side wall, and this circulating region narrows the main stream flow tube at the slot exit. This contraction accelerates the flow at the left half of the slot exit plane, and creates a low-pressure region over the left side wall edge, as shown in Fig. 12. The pressure difference between the right and the left side wall near the slot exit is 0.2–0.3 MPa. The slot depth is 480 mm. The region of the pressure difference is approximately $200(y) \times 40(x) = 8000$ mm^2. The arm length is about 0.9 m. Therefore, the roll torque for one slot estimated from these figures is 2160 N · m. Thus, the total for all seven slots is around 15 kN · m, and is about the same level of the evaluation of Eq. (22).

It should be noted that, in cases of $t = 1.6$ s, the roll torque is in the opposite direction as seen in Fig. 7. The streamlines also circle in the opposite direction to those shown in Fig. 8.

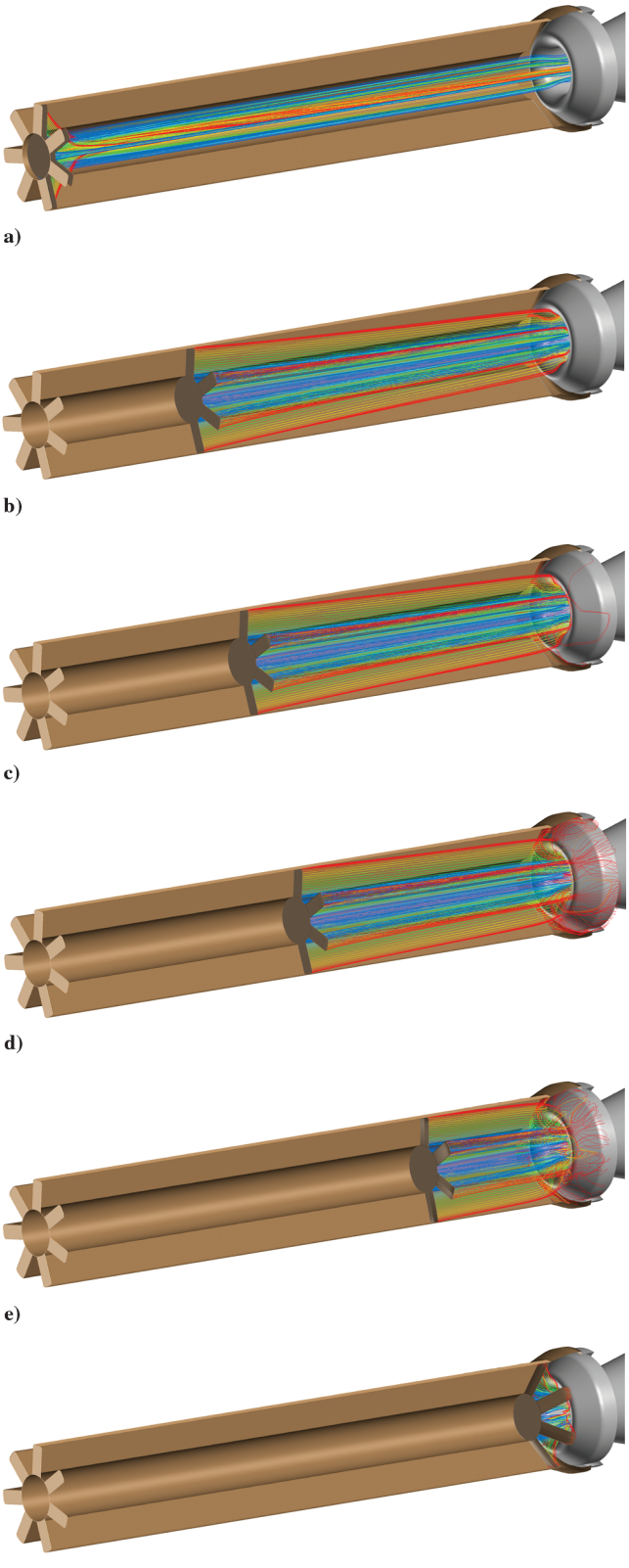

Fig. 14 Colored stream lines shed from the burning surface at representative axial locations, $t = 5$ s (perspective view): a) $x/L = 0.015$, b) $x/L = 0.30$, c) $x/L = 0.40$, d) $x/L = 0.50$, e) $x/L = 0.74$, f) $x/L = 0.94$.

E. Flowfield of Small-Torque Generation

As the representative of the small-torque solution, the case of $t = 5$ s is discussed. Figure 13 shows the streamlines viewed from $x = -\infty$ and Fig. 14 shows those from the perspective view. The major difference from the large-torque solution is that there is no circling flow around the inlet, but the streams shed from the bottom of the slot go out and impinge on the inlet surface, and turn to the left and the right, nearly symmetrically. Moreover, one of these streamlines impinges with one coming from a neighboring slot and turns quickly and goes out into the bore region (see Figs. 13c–13f). Therefore, there is not much interaction between the slot jet with the side wind at the slot exit facing the aft cavity (see Figs. 15 and 16). As a result, no pressure difference occurs, as shown in Fig. 17.

F. Mechanism of Large Roll-Torque Generation and Recommendation

As has been observed in the simulation results, roll torque is considered to be generated by the interaction of the circling flow and the slot jet at the slot exit facing the aft-end cavity. Such interaction becomes strong if the nozzle-submergence cavity is narrow and, at the same time, the axial slot is long, narrow, and deep. The slot exit radial position relative to the nozzle inlet is also important. In this

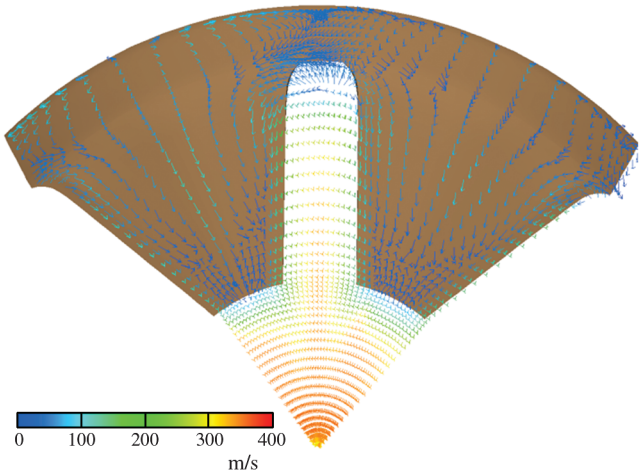

Fig. 15 Velocity field in the interfacing surface between the aft-end cavity and the propellant grain, $t = 5$ s.

case, it is also fitted to produce impingement of the slot jet on the nozzle inlet and, with a narrow flow passage in the submergence region, some imbalance of the symmetrical colliding reverse flows unstably, grows into a circling flow around the nozzle inlet, and reaches a steady circulation.

Such narrow submergence may be a result of an improvement in the propellant-loading ratio and the long, deep slot may be a result of chasing the heavy lift immediately after ignition, which is also to reduce gravity loss, considering the fact that the M-14 is a first-stage motor. It is, in general, reasonable to seek such a design to improve performance, but the recommendation here is to consider carefully the 3-D flow effect in the aft-end cavity. Depending on the design, the mechanism of the roll-torque generation found in the present numerical experiment can become easily high because it is based on the local pressure difference between the grain slot walls.

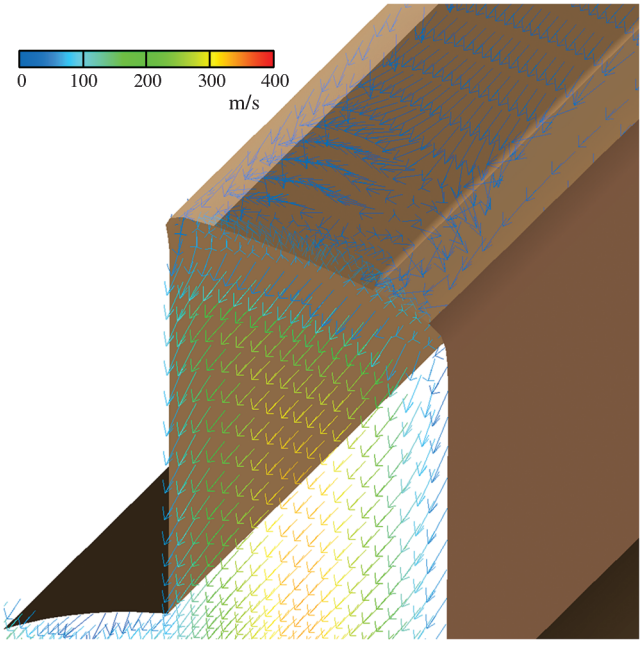

Fig. 16 Velocity distribution near the slot exit to the aft-end cavity, $t = 5$ s.

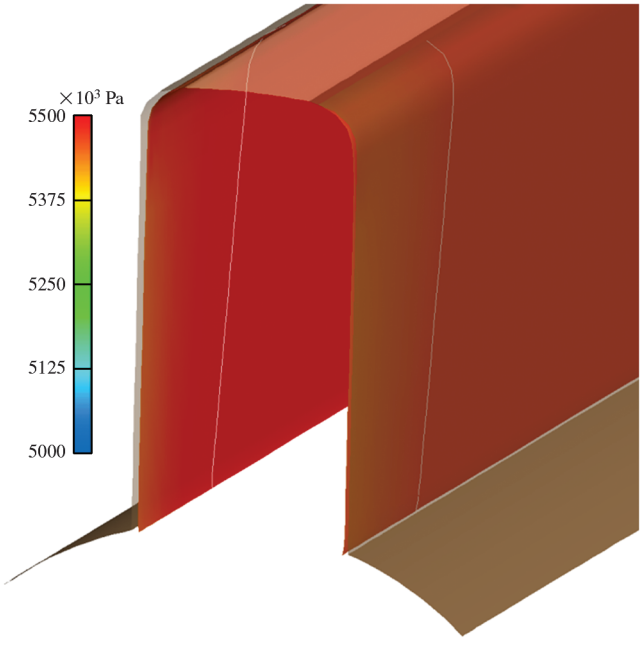

Fig. 17 Pressure distribution around the slot exit to the aft-end cavity, $t = 5$ s.

IV. Conclusions

From the current numerical simulation, we envisaged a mechanism of large roll-torque generation in an operating SRM with axially slotted propellant grain and a narrow submergence region around a noncanted nozzle inlet, as is the case with the M-14 motor of the M-V rocket. In general, these design points might be the result of seeking an improvement in LV performance, but the current simulation suggested that it also is important to consider the unstable nature of the aft-end cavity flow, as it has the potential to generate a very large roll torque to the limit of the steady state. In reality, there are various other factors to consider, especially the turbulent energy dissipation effect and the two-phase flow effect. Despite that, the current results serve to give insight into an understanding of the mechanism of the roll-torque generation.

Acknowledgments

The authors wish to extend their special thanks to Hideo Miyachi and Saori Sakamoto. Most of the numerical simulations were conducted using supercomputers of the Institute of Space and Astronautical Science of the Japan Aerospace Exploration Agency. This research was supported by Japan Aerospace Exploration Agency grants U5-4K2-USRPJ-1002 and B-UA-08-4K2-UHA1U-1002.

References

[1] Mayhue, R. J., "NASA Scout ST-1 Flight Test Results and Analysis, Launch Operations, and Test Vehicle Description," NASA TN D-1240, 1962.

[2] Swithenbank, J., and Sotter, G., "Vortices in Solid Propellant Rocket Motors," *AIAA Journal*, Vol. 1, No. 7, 1963, pp. 1682–1684. doi:10.2514/3.1891

[3] Swithenbank, J., and Sotter, G., "Vortex Generation in Solid Propellant Rocket," *AIAA Journal*, Vol. 2, No. 7, 1964, pp. 1297–1302. doi:10.2514/3.2535

[4] Flandro, G. A., "Roll Torque and Normal Force Generation in Acoustically Unstable Rocket Motors," *AIAA Journal*, Vol. 2, No. 7, 1964, pp. 1303–1306. doi:10.2514/3.2536

[5] Flandro, G. A., "Rotating Flows in Acoustically Unstable Rocket Motors," Ph.D. Thesis, California Inst. of Technology, Pasadena, CA, 1967.

[6] Yang, J. Y. S., and Flandro, G. A., "Head-End Secondary Flows in Solid-Propellant Rockets due to Transverse Acoustic Waves," *AIAA Journal*, Vol. 9, No. 6, 1971, pp. 1125–1129. doi:10.2514/3.6331

[7] Knauber, R. N., "Roll Torques Produced by Fixed-Nozzle Solid Rocket Motors," *Journal of Spacecraft and Rockets*, Vol. 33, No. 6, 1996, pp. 789–793. doi:10.2514/3.26839

[8] Williams, T., and Cannon, S., "Ares I First Stage Design, Development, Test, and Evaluation," 57th International Astronautical Congress, International Astronautical Federation Paper IAC-06-D2.7.02, 2006.

[9] Davis, S. R., Robinson, K. F., and Askins, B. R., "The Ares I-X Flight Test: Paving the Road for the Ares I Crew Launch Vehicle," 43rd AIAA/ASME/SAE/ASEE Joint Propulsion Conference and Exhibit, AIAA Paper 2007-5835, 2007.

[10] Roux, C. R., and Cruciani, I., "Roll Coupling Effects on the Stability Margins for VEGA Launcher," AIAA Atmospheric Flight Mechanics Conference and Exhibit, AIAA Paper 2007-6630, 2007.

[11] Bisi, L., Scaccia, Al., and Barbagallo, D., "Roll Torque Analysis for a Solid-Propellant Single-Body Launcher," 59th International Astronautical Congress, International Astronautical Federation Paper IAC-08-C4.2.11, 2008.

[12] Matsuo, H., Kohno, M., and Onoda, J., "Development of M-V Rocket," 48th International Astronautical Congress, International Astronautical Federation Paper IAF-97-V.1.08, 1997.

[13] Onoda, J., Sato, E., Inatani, Y., Minesugi, K., Shimada, T., and Nakamura, M., "Return to the Flight of M-V Rocket," 55th International

Astronautical Congress, International Astronautical Federation Paper IAC-04-IAF-V.1.02, 2004.
[14] Shimada, T., "Unique Phenomena Resulting from Three-Dimensional Flows Inside Solid Propellant Rockets," 57th International Astronautical Congress, International Astronautical Federation Paper IAC-06-C4.3.02, 2006.
[15] Shimada, T., and Sekino, N., "Roll Torque Induced by Star-Perforated Motor Internal Flow," 58th International Astronautical Congress, International Astronautical Federation Paper IAC-07-C4.2.07, 2007.
[16] Shimada, T., Sekiguchi, M., and Sekino, N., "Flow Inside a Solid Rocket Motor with Relation to Nozzle Inlet Ablation," *AIAA Journal*, Vol. 45, No. 6, 2007, pp. 1324–1332.
doi:10.2514/1.22952

J. Oefelein
Associate Editor